Polariton $\mathbb{Z}$ Topological Insulator

A. V. Nalitov, D. D. Solnyshkov, and G. Malpuech
Institut Pascal, PHOTON-N2, Université Clermont Auvergne, Blaise Pascal University, CNRS, 24 Avenue des Landais, 63177 Aubière Cedex, France
(Received 13 November 2014; published 16 March 2015)

We demonstrate that honeycomb arrays of microcavity pillars behave as an optical-frequency two-dimensional photonic topological insulator. We show that the interplay between the photonic spin-orbit coupling natively present in this system and the Zeeman splitting of exciton polaritons in external magnetic fields leads to the opening of a nontrivial gap characterized by a $C = \pm 2$ set of band Chern numbers and to the formation of topologically protected one-way edge states.

DOI: 10.1103/PhysRevLett.114.116401 PACS numbers: 71.36.+c, 03.65.Vf

The history of topological insulators (TIs) dates back to the discovery of the quantum Hall effect (QHE) by Klaus von Klitzing in 1980 [1]. In his experiment, a strong magnetic field pinned the conduction-band electrons to the Landau levels, opening a band gap in the bulk and thus converting an electron conductor to an insulator. The edge electron states, on the contrary, carried one-way currents, protected from backscattering and responsible for the integer Hall conductance [2]. This is an example of a $\mathbb{Z}$ topological insulator. The classification that allowed distinguishing this phase from a conventional band insulator is based on the Chern topological invariant [3], an integer number characterizing the band structure in terms of the Berry phase.

A whole new family of TI materials with different sets of topological invariants and symmetries were later proposed and discovered [4]. Graphene has a special place in this family: it allowed the observation of the QHE at room temperature [5] and played a role of a model system for QHE without net magnetic flux [6] and the quantum spin Hall effect (QSHE) [7]. The latter is associated with topologically protected boundary spin currents and is characterized by a nonzero $\mathbb{Z}_2$ invariant stemming from the spin-orbit interaction (SOI) for electrons [8] (without external magnetic field). These spin currents in the $\mathbb{Z}_2$ TI are formed from two spin components propagating in opposite directions, contrary to the $\mathbb{Z}$ TI, where both spin components propagate in the same direction, the other being forbidden. Although the extremely small SOI has not allowed us to observe QSHE in graphene, it was later demonstrated in various two-dimensional (2D) and three-dimensional structures [9,10]. A Floquet TI having a topologically nontrivial gap was realized in a 2D heterostructure under a microwave-range electromagnetic irradiation [11].

Many promising implementations of topological phases in bosonic systems were recently proposed in honeycomb photonic gyromagnetic waveguides [12–14], coupled microcavities [15], coupled cavity rings [16], coupled waveguides with a spatial modulation [17], and photonic waveguides (out of the optical range) based on metamaterials with bianisotropic behavior [18,19]. Finally, optical QHE due to artificial gauge fields [20] was predicted in microcavity lattices.

Cavity polaritons result from the strong coupling between confined cavity photons and quantum well (QW) excitons. They are photonic states, but with an exciton fraction, making them strongly interacting—a feature at the heart of polariton Bose-Einstein condensation and of the quantum fluid behavior of a polariton gas [21]. In this Letter, we exploit other polariton features: the exciton (and thus polariton) Zeeman splitting [22,23] and the polarization splitting of photonic modes, interpreted as an effective SOI for polaritons [24–27]. In-plane potentials for photons can also be created by using metal deposition [28], surface acoustic waves [29], or patterning of the planar structure [30]. All these ingredients give the polariton platform a unique flexibility to engineer the photonic properties of structures at optical frequencies. A first proposal of using polaritons to create a photonic topological insulator was given in Ref. [31], where the authors introduced winding in the system via the phase of the light matter coupling depending on the polar angle (vortical coupling), whose feasibility has not yet been demonstrated experimentally.

In this work, rather than creating artificial gauge fields or using weak gyromagnetic optical activity to break the time-reversal symmetry, we propose to exploit the natural susceptibility of microcavity polaritons to the magnetic field and the effective SOI acting on polaritons in photonic nanostructures. We consider polaritons in a honeycomb potential, called polariton graphene [30,32]. We demonstrate that a real magnetic field applied along the growth axis allows the formation of an original $\mathbb{Z}$ topological insulator with band Chern numbers $C_m = \pm 2$. We find the protected edge states by tight-binding calculation of the honeycomb microcavity stripe eigenstates. This result is confirmed by direct numerical simulations. We stress that contrary to Ref. [31], our proposal is based on existing ingredients all having the proper magnitude for the effect to be observable experimentally.

 © 2015 American Physical Society

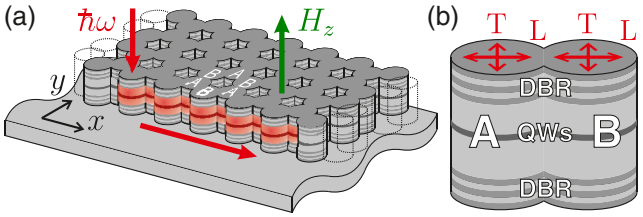

FIG. 1 (color online). (a) Topologically protected light propagation through an edge of polariton topological insulator. The polariton graphene considered is based on an etched planar microcavity. The cavity is constituted by two distributed Bragg reflectors (DBRs) sandwiching a cavity with embedded QWs. The energy splitting existing between TE and TM polarized modes provides the photonic SOI. The application of a real magnetic field perpendicular to the x-y plane of the structure opens the nontrivial gap. Edge modes are one-way propagative modes that cannot elastically scatter to the bulk states. In a stripe geometry, normally incident light is guided either clockwise or anticlockwise, depending on the external magnetic field sign. (b) A zoom view of two coupled microcavity pillars A and B; L and T localized polariton modes are linearly polarized along and transversely to the AB axis between the centers of the pillars.

Tight-binding model.—We first consider a photonic molecule consisting of two coupled pillars A and B [Fig. 1(b)] and find its 4×4 Hamiltonian in the following basis of states $|A,L\rangle$, $|A,T\rangle$, $|B,L\rangle$, $|B,T\rangle$. Here, A/B define the pillar at which a state is localized, while L/T name the polarization of a state—either longitudinal or transverse to the AB axis connecting the pillars. Because of the circular symmetry of the pillars and their identity, all basis states are degenerate; we set their energy to 0. In the absence of external magnetic field, within each pillar linearly polarized states are uncoupled; therefore, we find that 2×2 diagonal blocks of the Hamiltonian consist of zeros. A polarization splitting arises from the difference of reflection coefficients of the DBRs for two polarizations (TE/TM or L/T) [33]. This splitting acts on a propagating polariton (thus affecting the off-diagonal matrix elements) as an effective field with absolute value proportional to squared momentum, which can be described by assigning two effective masses $m_L < m_T$ to the new eigenstates, polarized longitudinally and transversely to propagation direction. We estimate potential barrier due to size quantization at narrow junction between the pillars as $V_{L(T)} = \pi^2\hbar^2/2m_{L(T)}w^2$, where w is the junction width. Note that the barrier value depends on the mass in direction, orthogonal to the AB axis. For the state $|A,L(T)\rangle$, wave function tail at pillar B is determined by tunnel extinction coefficient $\kappa_{L(T)} = \hbar^{-1}\sqrt{2m_{L(T)}(V_{T(L)} - E)}$. Therefore, we find that the nondiagonal blocks have different matrix elements $-J_{L,T}$, $J_L > J_T$ at their diagonals, whose values depend on overlaps of corresponding wave functions. The off-diagonal terms are zero, because all sources of spin conversion other than LT splitting are neglected. A transfer to the basis of circularly polarized states gives (see the Supplemental Material [34]) $-J = -(J_L + J_T)/2$ matrix elements at diagonals and introduces off-diagonal terms $-\delta J = -(J_L - J_T)/2$.

Starting from this Hamiltonian, we construct the polaritonic graphene [Fig. 1(a)] effective Hamiltonian in nearest-neighbor approximation. A state of the polariton graphene can be described by a bispinor $\Phi = (\Psi_A^+, \Psi_A^-, \Psi_B^+, \Psi_B^-)^{\mathrm{T}}$, with $\Psi_{A(B)}^{\pm}$ the wave functions of the two sublattices and two spin components. We account for the magnetic field via Zeeman splitting Δ of states, localized at a pillar. Finally, the effective Hamiltonian in the presence of a real magnetic field applied along the z direction reads (see the Supplemental Material [34])

$$H_{\mathbf{k}} = \begin{pmatrix} \Delta\sigma_z & F_{\mathbf{k}} \\ F_{\mathbf{k}}^{\dagger} & \Delta\sigma_z \end{pmatrix}, \qquad \Delta = |x|^2 g_X \mu_B H_z/2, \tag{1}$$

where σ_z is the Pauli matrix, x is the excitonic Hopfield coefficient, g_X is the effective g factor for the 2D exciton, μ_B is the Bohr magneton, and H_z is the applied magnetic field, giving rise to polariton Zeeman splitting Δ.

$$F_{\mathbf{k}} = -\begin{pmatrix} f_{\mathbf{k}} J & f_{\mathbf{k}}^{+}\delta J \\ f_{\mathbf{k}}^{-}\delta J & f_{\mathbf{k}} J \end{pmatrix}, \tag{2}$$

where complex coefficients $f_{\mathbf{k}}, f_{\mathbf{k}}^{\pm}$ are defined by

$$f_{\mathbf{k}} = \sum_{j=1}^{3} \exp(-i\mathbf{k}\mathbf{d}_{\varphi_j}),$$

$$f_{\mathbf{k}}^{\pm} = \sum_{j=1}^{3} \exp\left(-i[\mathbf{k}\mathbf{d}_{\varphi_j} \mp 2\varphi_j]\right),$$

and $\varphi_j = 2\pi(j-1)/3$ is the angle between the horizontal axis and the direction to the jth nearest neighbor of a type-A pillar. J is the polarization-independent tunneling coefficient, whereas δJ is the SOI-induced polarization-dependent term. Without the magnetic field, the Hamiltonian (1) can be exactly diagonalized [26]. The energy dispersions obtained are relatively close to those of bilayer graphene [35] and of a monolayer graphene in the presence of Rashba SOI [36]. The polarization texture of the eigenstates is, however, different (Rashba vs Dresselhaus).

The dispersion close to the $\mathbf{K}$ point is shown in the dashed lines on Fig. 2(a). Under the effect of SOI, the Dirac point transforms into four inverted parabolas. Two parabolas are split off, while the two central ones cross each other. It is instructive to consider the eigenstates exactly at the Dirac points. At the K point, the eigenstates of the two central parabolas are fully projected on Ψ_A^- and Ψ_B^+, respectively, whereas at the K' point they project on Ψ_A^+ and Ψ_B^-, respectively. Let us now qualitatively consider the consequence of a finite Zeeman splitting. As sketched in Fig. 2(b), the degeneracy between the states in the crossing points of two branches (dashed lines) is lifted by 2Δ, and

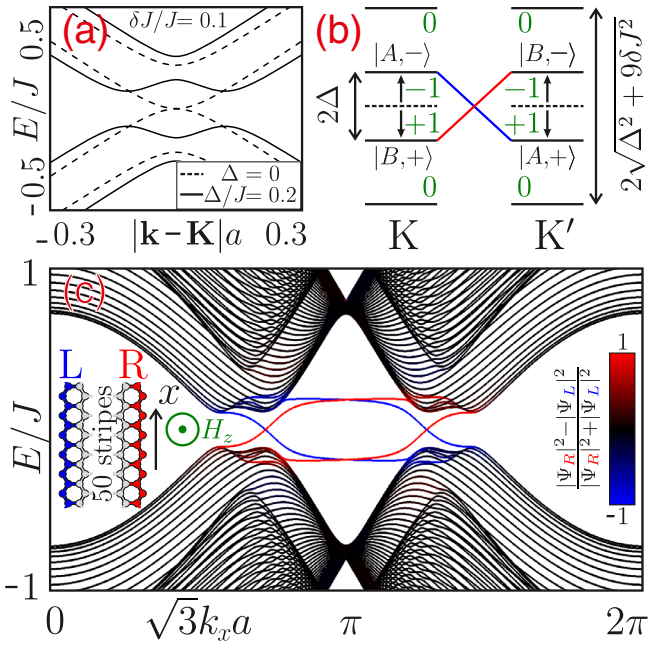

FIG. 2 (color online). Nontrivial band structure of the polariton graphene stripe in an external magnetic field. (a) Bulk energy dispersion without (dashed lines) and with (solid lines) magnetic field. (b) Illustration of degeneracy lifting in K and K' points. Because of coupling between sublattice and polarization, states localized on one sublattice go up in energy at one point and down in the other. Chern numbers at each point are shown in green. (c) Numerical calculation of eigenstates: edge states are marked with color. Direction of their propagation is given by the sign of the product $H_z g_X$ and is protected from both backscattering and scattering into the bulk.

the states split off by the SOI are further shifted. At the K (K') point, the "valence" band is formed from the $B(A)$ pillars and the "conduction" band is formed from the $A(B)$ pillars. The reversed order of the band in the basis of the sublattices signifies a topological nontriviality of the gap [4]. In the spin basis, however, the valence and conduction bands are equivalent at K and K', unlike the $\mathbb{Z}_2$-topological insulator [4].

The result of the complete diagonalization of the Hamiltonian (1) is plotted with solid lines in Fig. 2(a). As expected, it shows an energy gap, saturating to $E_g \sim 3\delta J$ at $|\Delta| \sim \delta J$. Without SOI ($\delta J = 0$), the application of a magnetic field does not open any gap, as it keeps the symmetry between K and K' valleys, while breaking the symmetry between the spin projections on the z axis. The band structure in this latter case is constituted by two graphene dispersions shifted in energy by the polariton Zeeman splitting.

The Chern numbers are numerically calculated from the Berry connection over the Brillouin zone [4],

$$C_m = \frac{1}{2\pi} \iint_{\mathrm{BZ}} \mathbf{B}_{\mathbf{k},m} d^2\mathbf{k}, \tag{3}$$

where m is the branch index, and the Berry curvature $\mathbf{B}_{\mathbf{k},m}$ is expressed in the effective Hamiltonian (1) and its eigenstates $|\Phi_{\mathbf{k},m}\rangle$ with corresponding energies $E_{\mathbf{k},m}$

$$\mathbf{B}_{\mathbf{k},m} = i \sum_{l \neq m} \frac{\langle \Phi_{\mathbf{k},m} | \nabla_{\mathbf{k}} H_{\mathbf{k}} | \Phi_{\mathbf{k},l} \rangle \times \langle \Phi_{\mathbf{k},l} | \nabla_{\mathbf{k}} H_{\mathbf{k}} | \Phi_{\mathbf{k},m} \rangle}{(E_{\mathbf{k},m} - E_{\mathbf{k},l})^2}. \tag{4}$$

Two inner branches, split by the interplay of external magnetic field and effective SOI, have nonzero Berry connections around K and K' points, each giving ± 1 contribution to the total band Chern number ± 2 [marked in green in Fig. 2(b)]. Outer branches, on the contrary, have zero Berry curvature over all reciprocal space.

As a consequence of bulk-boundary correspondence, a finite micropillar honeycomb structure has one-way propagating edge states. To demonstrate this, we use the same tight-binding approach to model a quasi-one-dimensional (1D) stripe of microcavity pillars, consisting of 50 zigzag chains.

To demonstrate one-way edge states in the tight-binding approach, we derive a $4N \times 4N$ Hamiltonian for a polariton graphene tape, consisting of N infinite zigzag stripes. For this, we set a basis of Bloch waves $\Psi^{\pm}_{A/B,n}(k_x)$, where n index numerates stripes, and k_x is the quasi-wave vector in the zigzag direction. The diagonal blocks describe coupling within one stripe and are derived in the same fashion as the Hamiltonian (1); coupling between stripes is accounted for in subdiagonal blocks.

Figure 2(c) shows the result of the band structure calculation. The degree of localization on edges is calculated from the wave function densities on the edge chains $|\Psi_L|^2$ and $|\Psi_R|^2$ (left and right, see inset) and is shown with color so that the edge states are blue and red. The propagation direction of these edge states is related to the direction of the external magnetic field: the photon edge current is either clockwise or anticlockwise depending on the signs of H_z and g_X. It is important that we deal with a real polariton current and not with a spin current. The polarization of the surface states is linear: both spin components propagate in the same direction.

The presented results were obtained for the most realistic case of rather small SOI ($\delta J/J = 0.1$). In this case, the dispersion topology in the absence of magnetic field is characterized by the trigonal warping effect, typical for bilayer graphene [35] and monolayer graphene with Rashba SOI [36]. It consists of the emergence of three additional Dirac cones in the vicinity of each Brillouin zone corner. However, at a critical strength of the spin-orbit interaction $\delta J = J/2$, a transition occurs in the topology of the dispersion: additional Dirac cones with opposite Chern numbers meet in pairs at the centers of Brillouin zone edges and recombine (see the Supplemental Material [34] for the dispersion). This leads to a change of the band Chern number set from $C_m = \pm 2$ to $C_m = \pm 1$.

Numerical simulations.— In order to demonstrate the feasibility of experimental observations and to confirm our predictions, we carry out a full numerical simulation, describing the time evolution of the polariton wave function by solving the spinor Schrodinger equation,

$$i\hbar\frac{\partial\psi_\pm}{\partial t} = -\frac{\hbar^2}{2m}\Delta\psi_\pm + U\psi_\pm - \frac{i\hbar}{2\tau}\psi_\pm \pm \Delta\psi_\pm + \beta\left(\frac{\partial}{\partial x} \mp i\frac{\partial}{\partial y}\right)^2\psi_\mp + \sum_j P_{j\pm}e^{-[(t-t_0)^2/\tau_0^2]}e^{-[(\mathbf{r}-\mathbf{r}_j)^2/\sigma^2]}e^{i(kr-\omega t)}, \quad (5)$$

where $\psi(\mathbf{r},t) = \psi_+(\mathbf{r},t), \psi_-(\mathbf{r},t)$ are the two circular components of the wave function, m is the polariton mass, and τ is the lifetime. Particles are created in three spots by pulsed quasiresonant pumping. The nVidia CUDA graphical processor was used to carry out the numerical integration of the 2D spinor Schrödinger equation. The high-resolution (1024×1024) honeycomb lattice potential $U(r)$ contains 23×30 elementary cells. The pillar size was 1.3 μm, and the center-to-center distance $d = 2.5$ μm. All energies are measured from the bottom of the polariton branch, which can shift with the magnetic field. Circular excitation allows us to be sure that all linearly polarized states are pumped with sufficient efficiency.

Figure 3 demonstrates qualitatively different behavior with and without the magnetic field (parameters of the simulations are given in the caption). Without the field ($\Delta = 0$), the excitation energy corresponds to propagating states, and the resulting expansion of polaritons is visible in Fig. 3(a). No gap is opened, and the particles created on the surface by the two corresponding pumps are rapidly expanding into the bulk: after only 20 ps, the intensity is distributed over a significant part of the sample. However, under an applied field giving $\Delta = 0.1$ meV, the excitation energy lies within a gap, which makes the injection in the center ineffective: no particles created by the pump are visible in the center after 100 ps. But the spots on the edges now become resonant with the surface states, which have appeared there, and their one-way propagation is visible in Fig. 3(b): after 100 ps, particles are about 25 μm away from the pump spots. Although particles are created with both positive and negative wave vectors along a given edge, they propagate in only one direction, which proves the one-way nature of the surface states. The transverse profile of these states shows an exponential decay (Supplemental Material [34]) with a characteristic length of $(2\kappa)^{-1} = 3.1 \pm 0.1$ μm, corresponding to the analytical estimate of the extinction coefficient $\kappa \approx \sqrt{2mE_g/\hbar^2}$ determined by the size of the gap E_g. Thus, the full numerical simulation confirms the predictions of the tight-binding model on the appearance of the gap in the presence of magnetic field (Supplemental Material [34]) and the formation of one-way surface states.

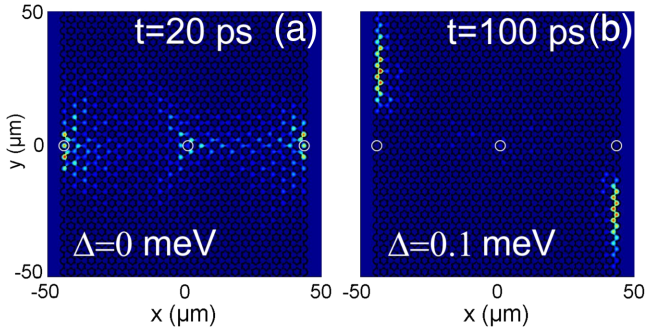

FIG. 3 (color online). Propagation of light in the conducting ($\Delta = 0$) and topological insulator phase ($\Delta \neq 0$). Calculated spatial distribution of emission intensity. (a) Rapid expansion of the bulk propagative states after 20 ps at $\Delta = 0$; (b) surface states after 100 ps at $\Delta = 0.1$ meV. White circles show the pumping spots located at $\mathbf{r}_j$. The contours of the potential are traced in black. The parameters are $\beta = \hbar^2(m_l^{-1} - m_t^{-1})/4m$ where $m_{l,t}$ are the effective masses of TM and TE polarized particles, respectively, and $m = 2(m_t - m_l)/m_t m_l$; $m_t = 5 \times 10^{-5} m_0$, $m_l = 0.95 m_t$, where m_0 is the free electron mass; $\tau_0 = 35$ ps, $\sigma = 1$ μm, $\omega = 1.6$ meV, $\tau = 25$ ps. Pumping P was circular polarized.

All the parameters used in the numerical simulations are entirely realistic. Indeed, the experimental realization of the effect has one important requirement: both δJ and Δ must exceed the radiative broadening, which is of the order of $1/(25\text{ ps}) \approx 30$ μeV [30], but also disorder-induced broadening, which is naturally included in our simulations through the finite spatial resolution. The total linewidth we get is 60 μeV, which is a good but realistic value. The photonic SOI finds its origin in the polarization splittings of photonic nanostructures. In etched planar cavities, it is induced by the TE-TM splitting [37] but also by strain and other structural effects that enhance the splittings up to 50–200 μeV in 1D ridges [38] or coupled pillar structures [39]. The Zeeman splitting between the spin components of polaritons can be of the order of 100–200 μeV at moderate magnetic fields (about 10 T) [22,23]. The size of the pillars we consider allows the formation of clearly separated s and p bands, so the presence of the excited states does not affect the lowest band. Moreover, as shown by our preliminary calculations, the p band [30] might be even more suitable for the observation of topologically protected surface states due to the increased SOI.

In summary, we have demonstrated that a polariton graphene under magnetic field becomes a $\mathbb{Z}$ topological insulator with protected edge states at optical frequencies. It resembles the QHE behavior of electrons and photons [15], both based on the appearance of Landau levels. However, its origin is different, being closer to the Haldane proposals [6,12]. The gap appears in our case due to the Zeeman splitting of electrically uncharged particles and specific spin-orbit coupling acting together similarly to spatially alternating magnetic fields [6,12]. The difference is underlined by the unique set of band Chern invariants $C_m = \pm 2$

(transforming into $C_m = \pm 1$ above a critical SOI, Supplemental Material [34]). From the point of view of symmetry, the topologically nontrivial gap is a manifestation of broken time-reversal and in-plane rotational symmetry by external magnetic field and effective SOI, respectively. The interacting nature of polaritons opens interesting possibilities of studying collective bosonic effects [21] in TIs. The spin anisotropy of these interactions [37] leads to self-induced Zeeman splitting, allowing a self-induced TI for a polarized polariton Bose-Einstein condensate. We also mention that a few days after our initial submission of our work on a preprint server [40], a similar, independent proposal, but based on the surface acoustic waves (SAW), was posted on the same server [41]. The advantage of etched structures over SAW is the reduced broadening due to the constant nature of the potential.

We acknowledge discussions with A. Poddubny, A. Amo, and J. Bloch. This work was supported by the ITN INDEX (289968), ANR Labex Ganex (ANR-11-LABX-0014), and IRSES POLAPHEN (246912).

[1] K. v. Klitzing, G. Dorda, and M. Pepper, Phys. Rev. Lett. **45**, 494 (1980).
[2] D. J. Thouless, M. Kohmoto, M. P. Nightingale, and M. den Nijs, Phys. Rev. Lett. **49**, 405 (1982).
[3] B. Simon, Phys. Rev. Lett. **51**, 2167 (1983).
[4] M. Z. Hasan and C. L. Kane, Rev. Mod. Phys. **82**, 3045 (2010).
[5] K. S. Novoselov, Z. Jiang, Y. Zhang, S. V. Morozov, H. L. Stormer, U. Zeitler, J. C. Maan, G. S. Boebinger, P. Kim, and A. K. Geim, Science **315**, 1379 (2007).
[6] F. D. M. Haldane, Phys. Rev. Lett. **61**, 2015 (1988).
[7] C. L. Kane and E. J. Mele, Phys. Rev. Lett. **95**, 226801 (2005).
[8] C. L. Kane and E. J. Mele, Phys. Rev. Lett. **95**, 146802 (2005).
[9] M. Konig, S. Wiedmann, C. Brne, A. Roth, H. Buhmann, L. W. Molenkamp, X.-L. Qi, and S.-C. Zhang, Science **318**, 766 (2007).
[10] D. Hsieh, D. Qian, L. Wray, Y. Xia, Y. S. Hor, R. J. Cava, and M. Z. Hasan, Nature (London) **452**, 970 (2008).
[11] N. H. Lindner, G. Refael, and V. Galitski, Nat. Phys. **7**, 490 (2011).
[12] F. D. M. Haldane and S. Raghu, Phys. Rev. Lett. **100**, 013904 (2008).
[13] Z. Wang, Y. D. Chong, J. D. Joannopoulos, and M. Soljačić, Phys. Rev. Lett. **100**, 013905 (2008).
[14] Z. Wang, Y. Chong, J. Joannopoulos, and M. Soljacic, Nature (London) **461**, 772 (2009).
[15] R. O. Umucalılar and I. Carusotto, Phys. Rev. Lett. **108**, 206809 (2012).
[16] M. Hafezi, E. A. Demler, M. D. Lukin, and J. M. Taylor, Nat. Phys. **7**, 907 (2011).
[17] M. C. Rechtsman, J. M. Zeuner, Y. Plotnik, Y. Lumer, D. Podolsky, F. Dreisow, S. Nolte, M. Segev, and A. Szameit, Nature (London) **496**, 196 (2013).
[18] A. B. Khanikaev, S. Hossein Mousavi, W.-K. Tse, M. Kargarian, A. H. MacDonald, and G. Shvets, Nat. Mater. **12**, 233 (2013).
[19] W.-J. Chen, S.-J. Jiang, X.-D. Chen, J.-W. Dong, and C. T. Chan, arXiv:1401.0367.
[20] T. Ozawa and I. Carusotto, Phys. Rev. Lett. **112**, 133902 (2014).
[21] I. Carusotto and C. Ciuti, Rev. Mod. Phys. **85**, 299 (2013).
[22] J. Fischer, S. Brodbeck, A. V. Chernenko, I. Lederer, A. Rahimi-Iman, M. Amthor, V. D. Kulakovskii, L. Worschech, M. Kamp, M. Durnev *et al.*, Phys. Rev. Lett. **112**, 093902 (2014).
[23] C. Sturm, D. Solnyshkov, O. Krebs, A. Lemaitre, I. Sagnes, E. Galopin, A. Amo, G. Malpuech, and J. Bloch, arXiv:1409.5112.
[24] A. Kavokin, G. Malpuech, and M. Glazov, Phys. Rev. Lett. **95**, 136601 (2005).
[25] C. Leyder, M. Romanelli, J. P. Karr, E. Giacobino, T. C. H. Liew, M. M. Glazov, A. V. Kavokin, G. Malpuech, and A. Bramati, Nat. Phys. **3**, 628 (2007).
[26] A. V. Nalitov, G. Malpuech, H. Terças, and D. D. Solnyshkov, Phys. Rev. Lett. **114**, 026803 (2015).
[27] V. G. Sala, D. D. Solnyshkov, I. Carusotto, T. Jacqmin, A. Lemaitre, H. Tercas, A. Nalitov, M. Abbarchi, E. Galopin, I. Sagnes *et al.*, arXiv:1406.4816.
[28] N. Y. Kim, K. Kusudo, C. Wu, N. Masumoto, A. Loffler, S. Hofling, N. Kumada, L. Worschech, A. Forchel, and Y. Yamamoto, Nat. Phys. **7**, 681 (2011).
[29] E. A. Cerda-Méndez, D. Sarkar, D. N. Krizhanovskii, S. S. Gavrilov, K. Biermann, M. S. Skolnick, and P. V. Santos, Phys. Rev. Lett. **111**, 146401 (2013).
[30] T. Jacqmin, I. Carusotto, I. Sagnes, M. Abbarchi, D. Solnyshkov, G. Malpuech, E. Galopin, A. Lemaitre, J. Bloch, and A. Amo, Phys. Rev. Lett. **112**, 116402 (2014).
[31] T. Karzig, C. Bardyn, N. Linder, and G. Refael, arXiv:1406.4156.
[32] K. Kusudo, N. Y. Kim, A. Löffler, S. Höfling, A. Forchel, and Y. Yamamoto, Phys. Rev. B **87**, 214503 (2013).
[33] G. Panzarini, L. C. Andreani, A. Armitage, D. Baxter, M. S. Skolnick, V. N. Astratov, J. S. Roberts, A. V. Kavokin, M. R. Vladimirova, and M. A. Kaliteevski, Phys. Rev. B **59**, 5082 (1999).
[34] See the Supplemental Material at http://link.aps.org/supplemental/10.1103/PhysRevLett.114.116401 for extra results of numerical simulations.
[35] E. McCann and M. Koshino, Rep. Prog. Phys. **76**, 056503 (2013).
[36] P. Rakyta, A. Kormányos, and J. Cserti, Phys. Rev. B **82**, 113405 (2010).
[37] I. A. Shelykh, A. V. Kavokin, Y. G. Rubo, T. C. H. Liew, and G. Malpuech, Semicond. Sci. Technol. **25**, 013001 (2010).
[38] G. Dasbach, C. Diederichs, J. Tignon, C. Ciuti, P. Roussignol, C. Delalande, M. Bayer, and A. Forchel, Phys. Rev. B **71**, 161308 (2005).
[39] M. Galbiati, L. Ferrier, D. D. Solnyshkov, D. Tanese, E. Wertz, A. Amo, M. Abbarchi, P. Senellart, I. Sagnes, A. Lemaitre *et al.*, Phys. Rev. Lett. **108**, 126403 (2012).
[40] A. Nalitov, D. Solnyshkov, and G. Malpuech, arXiv:1409.6564.
[41] C. Bardyn, T. Karzig, G. Refael, and T. Liew, arXiv:1409.8282.